Electronic Supplementary Material (ESI) for Journal of Materials Chemistry A.

Supplementary Information

Highly Porous Ni-P Electrode Synthesized by an Ultrafast Electrodeposition Process for Efficient Overall Water Electrolysis

DongHoon Song[a], Doosun Hong[a], YongKeun Kwon[a], HyoWon Kim[a], JaeWook Shin[a,b], Hyuck Mo Lee[a] and EunAe Cho[a]*

[a]*Department of Materials Science and Engineering, Korea Advanced Institute of Science and Technology (KAIST), 291 Daehak-ro, Yuseong-gu, Daejeon, 34141, Republic of Korea*

[b]*Advanced Battery Center, KAIST Institute for NanoCentury, Korea Advanced Institute of Science and Technology (KAIST), 291 Daehak-ro, Yuseong-gu, Daejeon 34141, Republic of Korea*

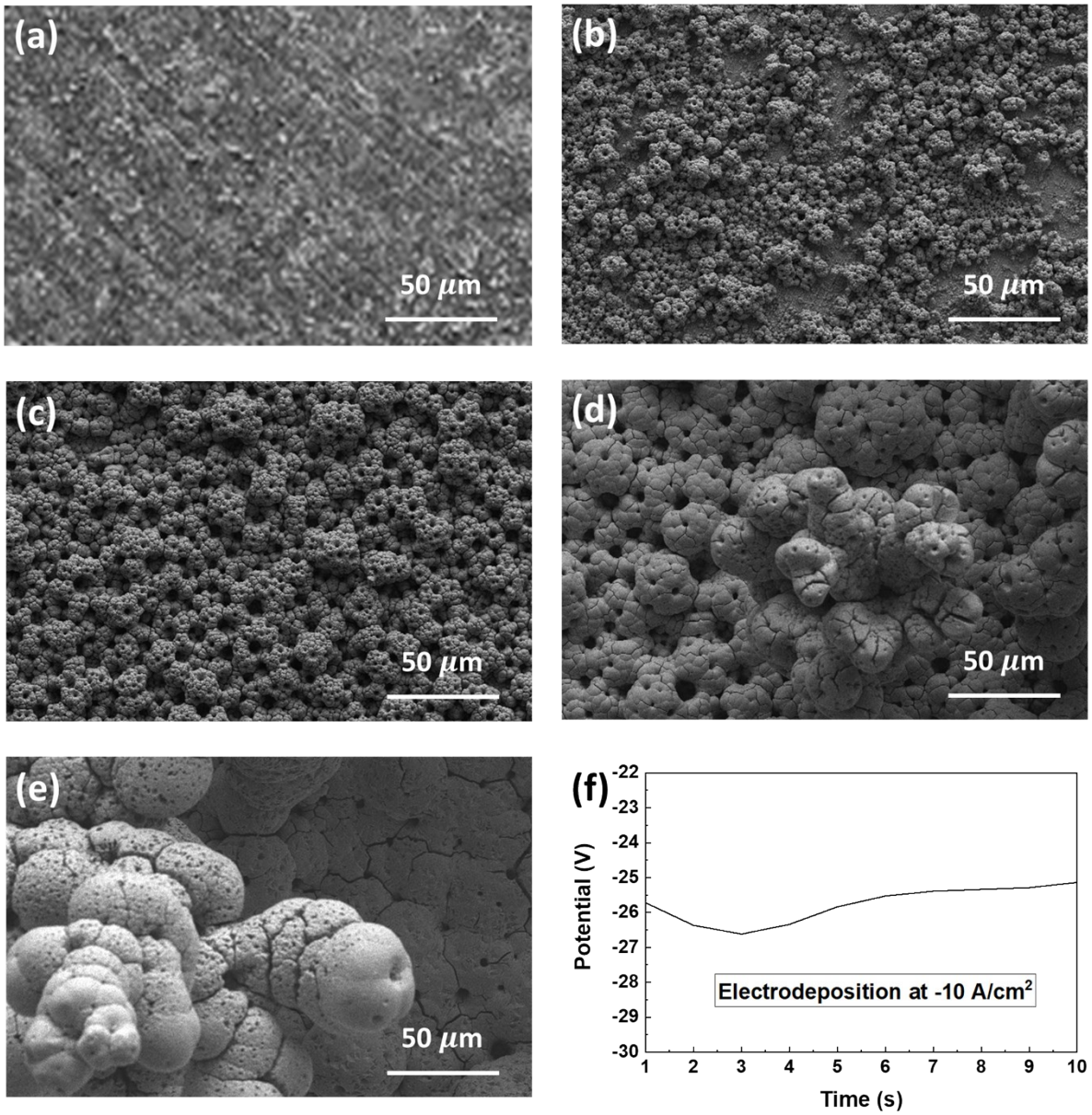

Figure S1. SEM images of the Ni-P electrodes deposited at -10 A/cm^2 for (a) 1, (b) 5, (c) 10, (d) 30, and (e) 60 seconds. (f) Voltage-time curve for the electrodeposition of Ni-P at -10 A/cm^2 during 10 seconds,

At the very early stage of the electrodeposition within 1 second, small Ni-P seed islands were formed on the surface of the substrate (Fig. S1a). After 5 seconds, Ni-P particles having a porous structure are observed with exposed substrate surfaces that are not covered with the Ni-P particles (Fig. S2b). After 10 seconds, the substrate surface is completely covered with the highly porous Ni-P layer (Fig. S1c). Upon further electrodeposition, denser Ni-P layers were formed with larger particles (Fig. S1d and e).

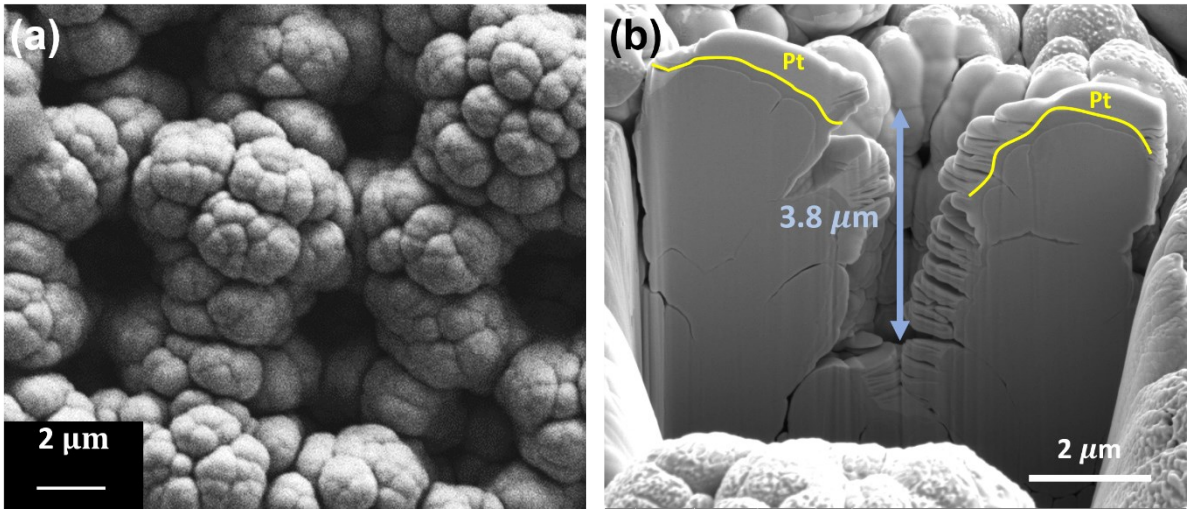

Figure S2. SEM images of the HP Ni-P; (a) surface and (b) cross sectional image in which the Pt layer was coated on top of the sample for protection from ion-beam damage during FIB milling.

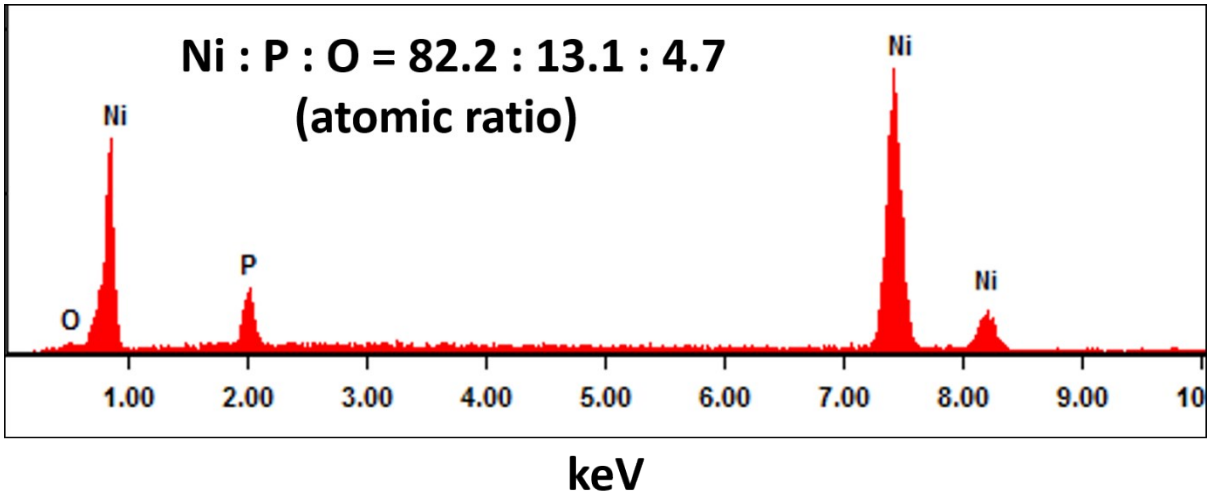

Figure S3. Spectra of SEM energy dispersive spectroscopy analysis of the HP Ni-P.

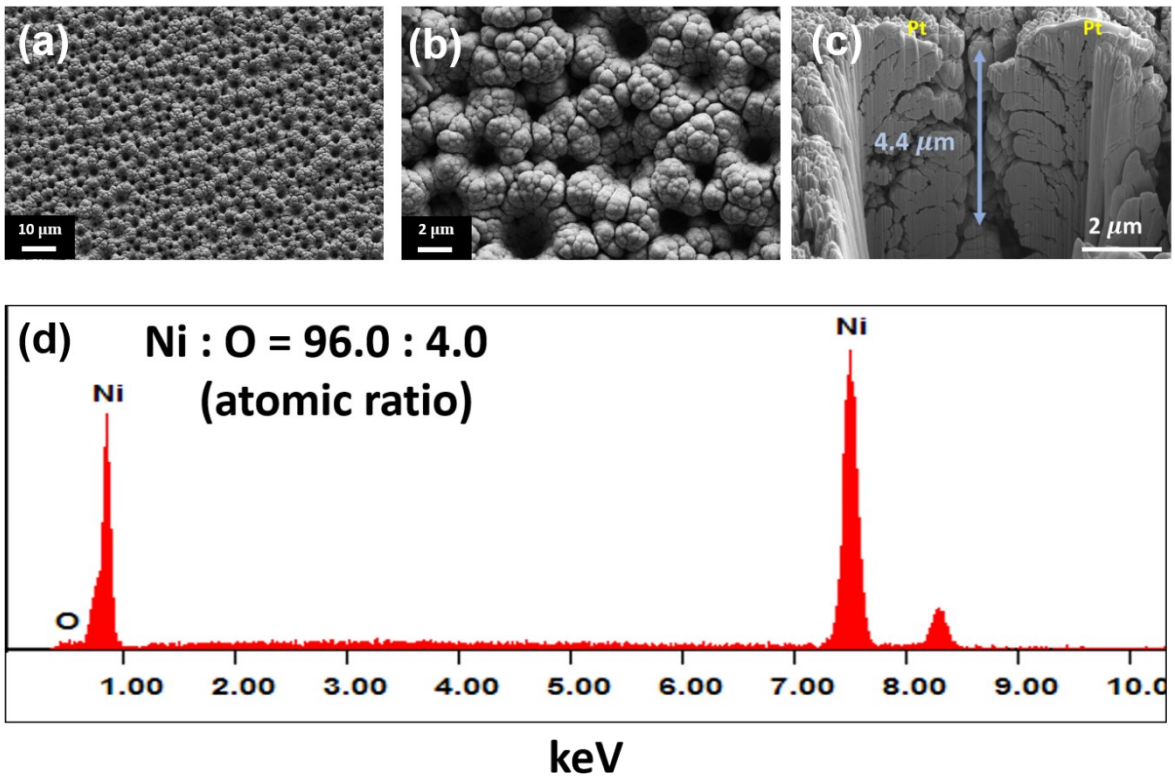

Figure S4. SEM images of the HP Ni; (a),(b) surface and (c) cross sectional image in which the Pt layer was coated on top of the sample for protection from ion-beam damage during FIB milling. (d) Spectra of SEM energy dispersive spectroscopy analysis of the HP Ni.

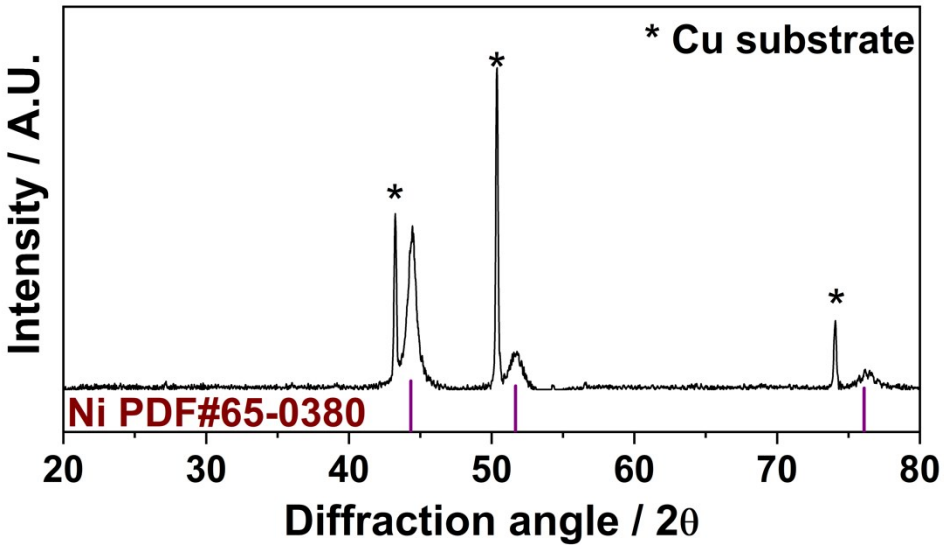

Figure S5. XRD pattern of the HP Ni.

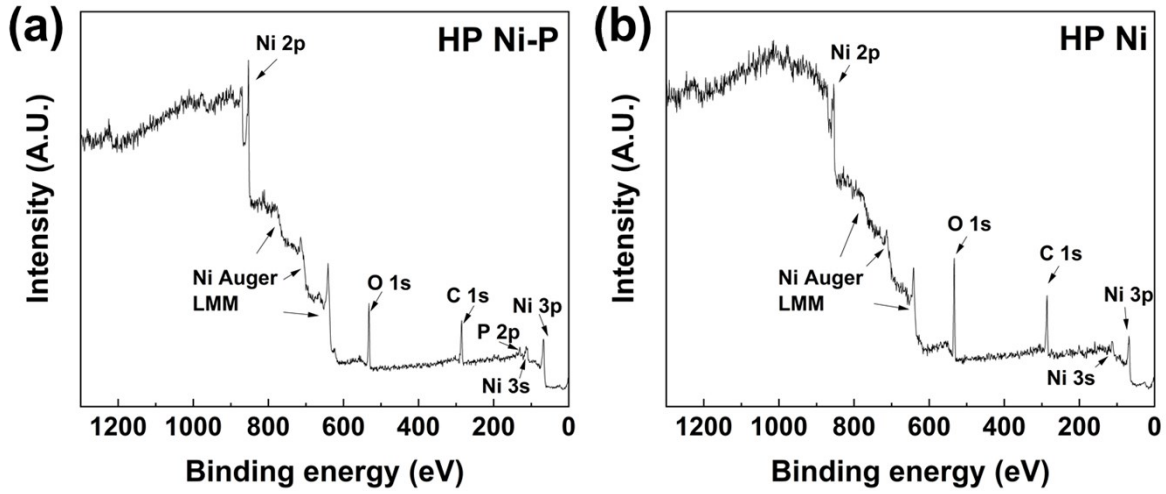

Figure S6. XPS survey spectra of (a) HP Ni-P and (b) HP Ni.

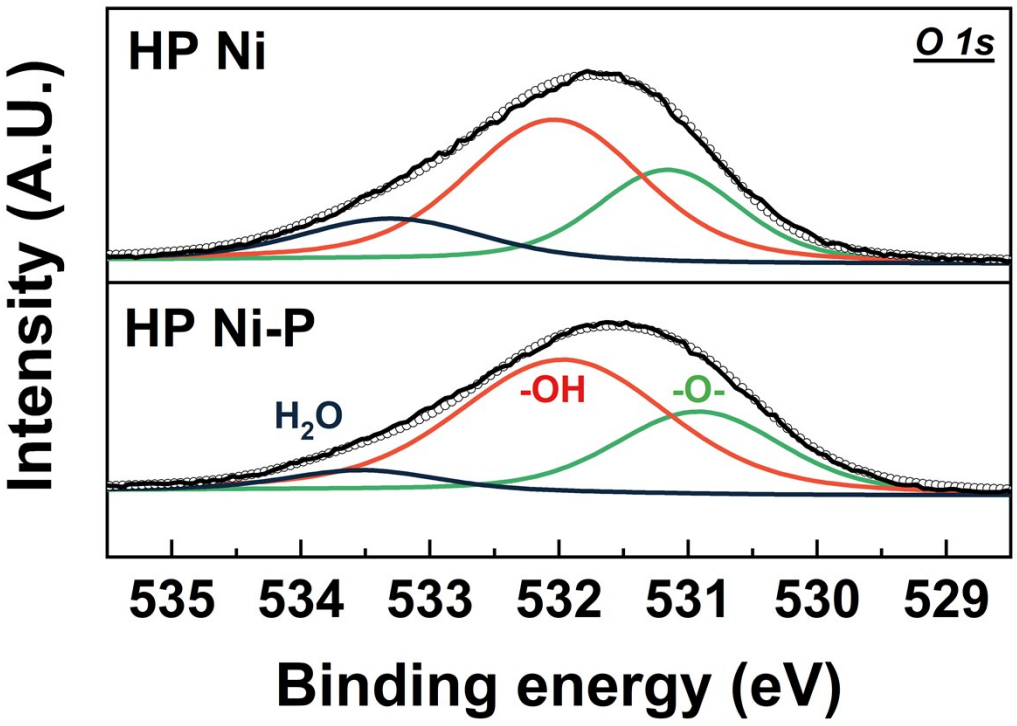

Figure S7. O 1s XPS spectra of the HP Ni and the HP Ni-P

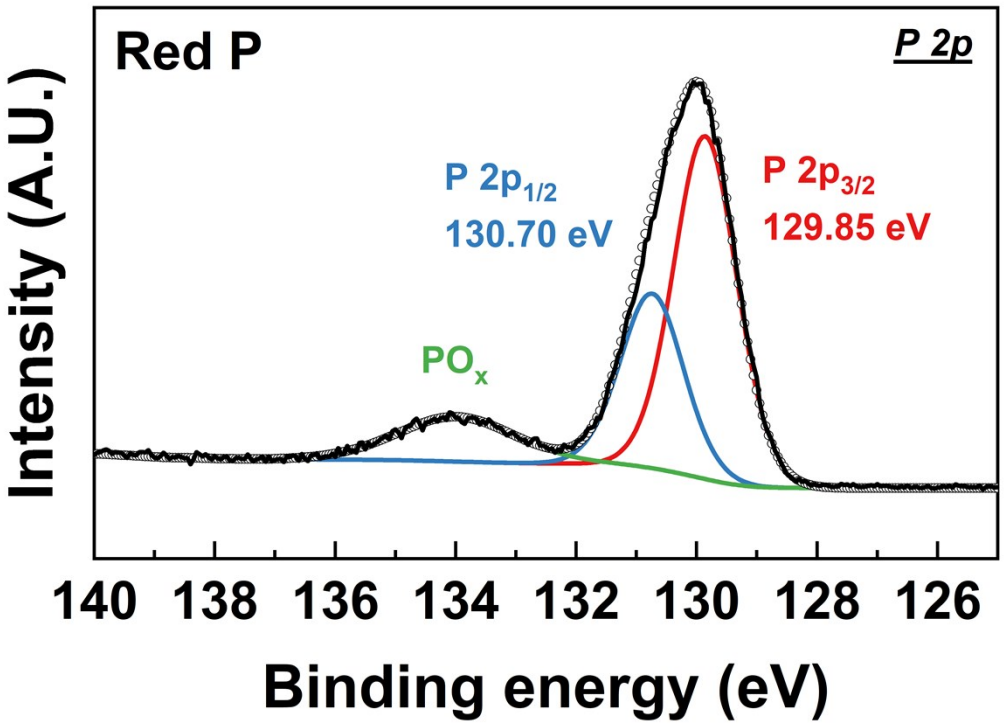

Figure S8. P 2p XPS spectrum of the red phosphorus.

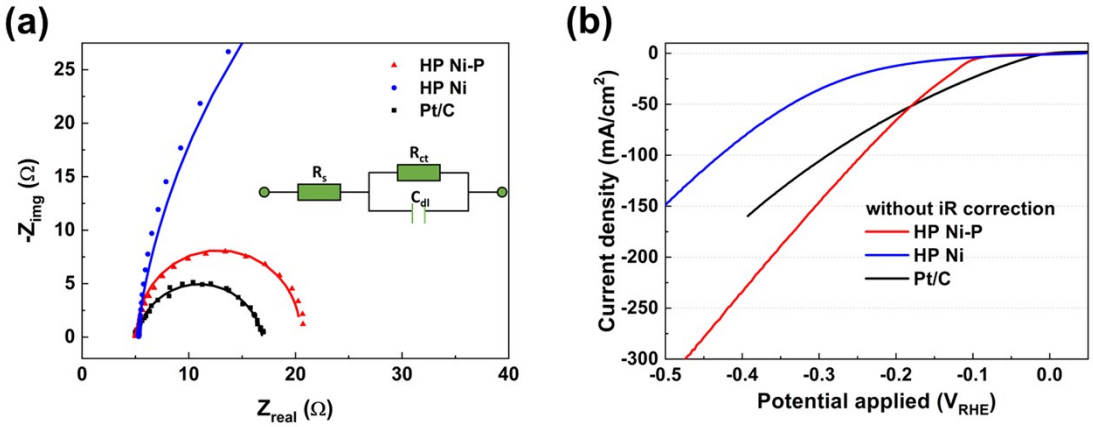

Figure S9. (a) Nyquist plots at -0.1 V_{RHE} and (b) HER polarization curves of the HP Ni-P, HP Ni, and commercial Pt/C in 1 M KOH without iR correction.

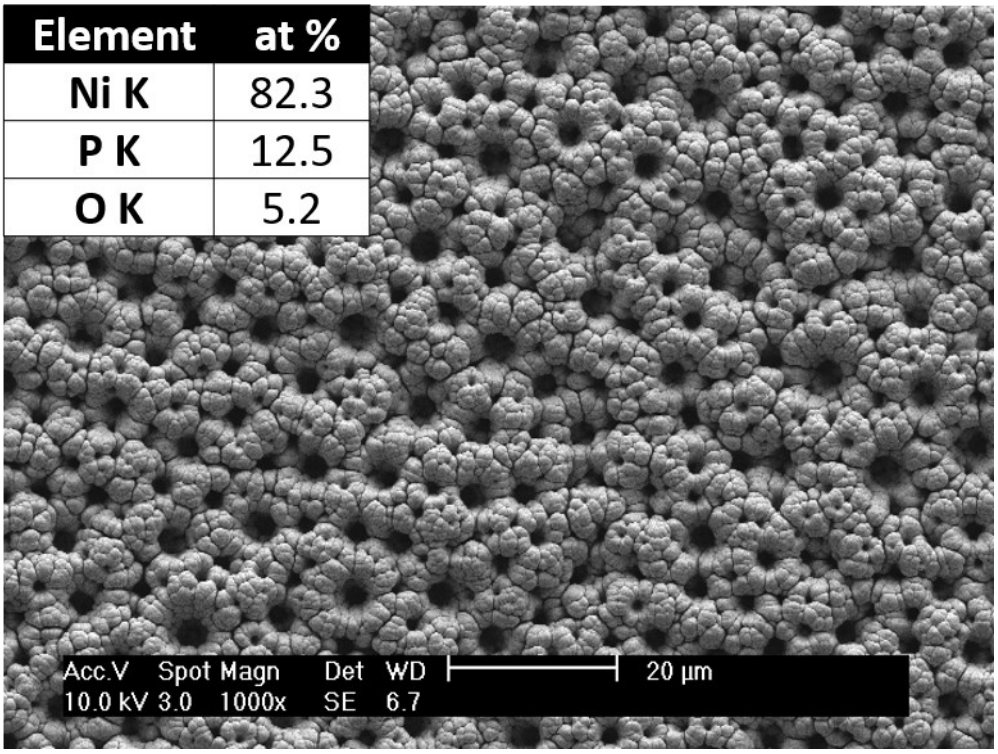

Figure S10. SEM image and elemental composition of the HP Ni-P after 10 h chronopotentiometry test at -100 mA/cm^2.

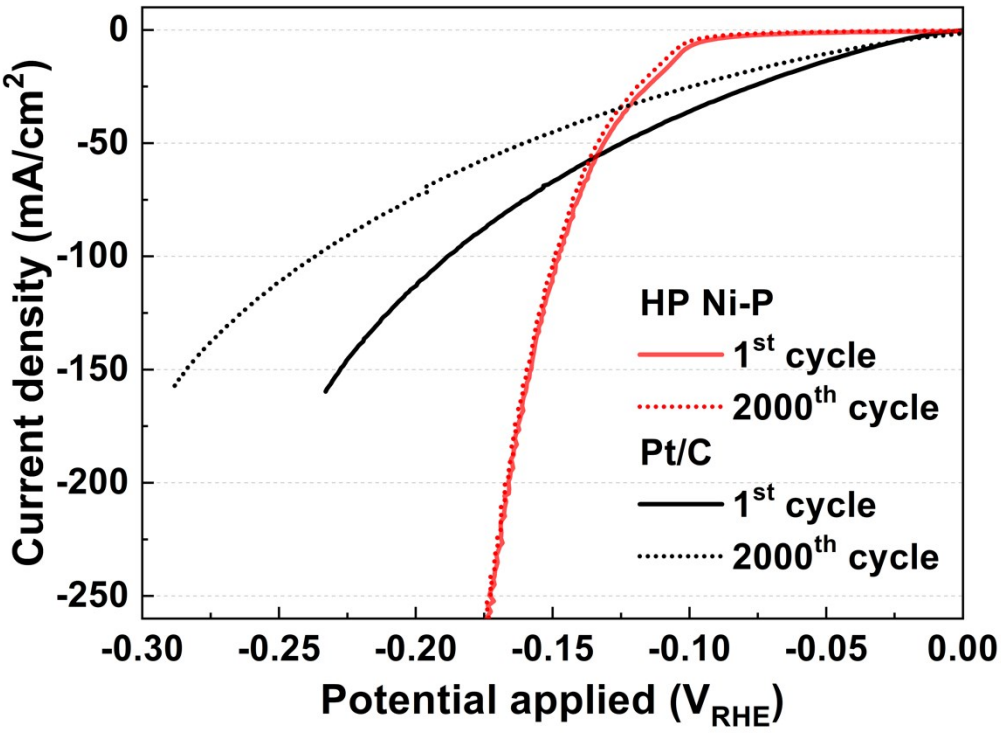

Figure S11. HER activities of the HP Ni-P and the Pt/C before and after the potential cycling test from 0 to -0.4 V_{RHE} at a scan rate of 100 mV/s for 2000 cycles in 1 M KOH.

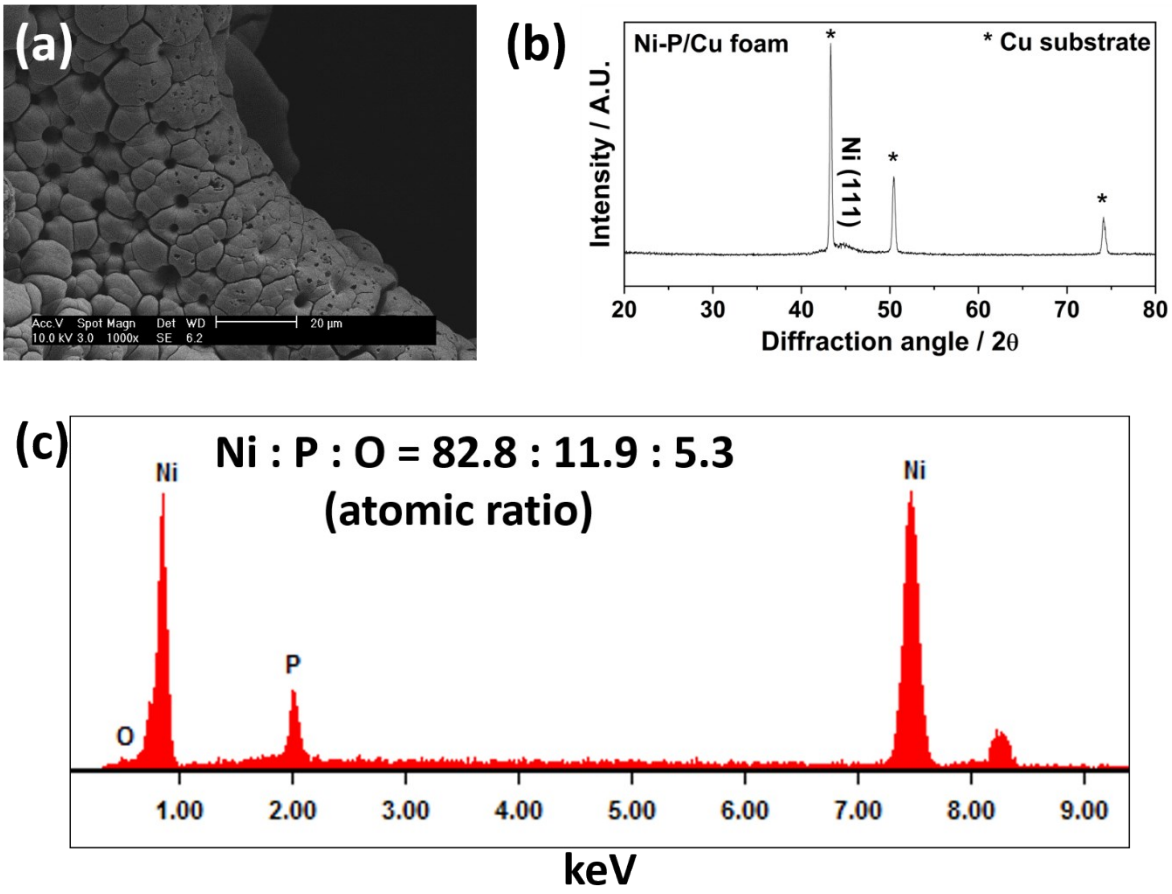

Figure S12. (a) SEM images of the HP Ni-P on Cu foam, (b) XRD pattern of the HP Ni-P on Cu foam, (c) Spectra of SEM energy dispersive spectroscopy analysis of the HP N-P on Cu foam.

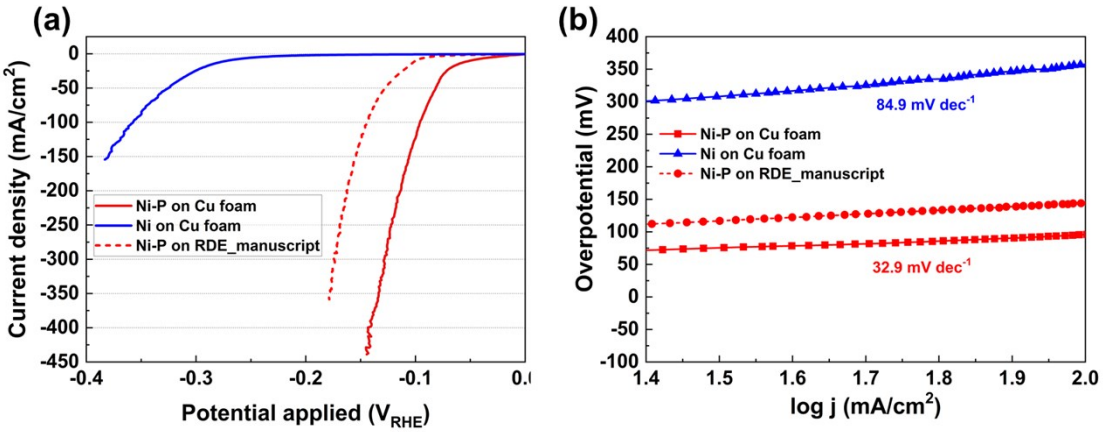

Figure S13. HER activities of the HP Ni-P deposited on Cu foam in 1 M KOH. (a) polarization curves, (b) corresponding Tafel plots.

Table S1. Comparison of HER catalytic activity and performance with the state-of-the-art transition-metal phosphide or phosphorus catalysts.

Electrocatalyst	Overpotential (mV) at 10 mA/cm^2	Overpotential (mV) at 100 mA/cm^2	Tafel slope (mV/dec)	Electrolyte
HP Ni-P on foam (This work)	**52**	**96**	**32.9**	**1 M KOH**
HP Ni-P on RDE (This work)	99	144	37.4	1 M KOH
$NiP_{1.92}Se_{0.08}$ [1]	119	205	81	1 M KOH
O-NiMoP2/NF [2]	31	134	62.1	1 M KOH
$Ni_{2(1-x)}Mo_{2x}P$/NF [3]	72	162	46.4	1 M KOH
FeP/Ni_2P/NF [4]	14	150	24.2	1 M KOH
Ni_2P/rGO [5]	142	300	58	1 M KOH
np-$Ni_{0.67}Fe_{0.33}P_5$ [6]	120	200	41.8	1 M KOH
NiP_2/NiO/CF [7]	131	250	94	1 M KOH
Porous Ni_2P [8]	168	-	63	1 M KOH
Ni-Co-P [9]	83	165	46.6	1 M KOH
$Ni_{11}(HPO_3)_8(OH)_6$/NF [10]	42	130	102	1 M KOH
O_3-V_{10}-Ni_2P [11]	108	280	72.3	1 M KOH
$NiCo_2P_x$/CNT [12]	42	130	57	1 M KOH
Ni_2P/NF [13]	-	205	68.9	1 M KOH
$Ni_{1.85}Fe_{0.15}P$ NSAS/NF [14]	106	200	89.7	1 M KOH
Ni_2P/Ni/NF [15]	98	165	72	1 M KOH
Ni_2P/NF [16]	220	-	-	1 M KOH
Co-P foam [17]	131	-	-	1 M KOH
CoP/C [18]	210	-	-	0.1 M KOH

Table S2. HER activities of the electrodeposited Ni-P catalysts.

Electrocatalyst	Overpotential at 10 mA/cm^2 (mV)	Overpotential at 100 mA/cm^2 (mV)	Tafel slope (mV/dec)	Loading amount (mg/cm^2)
HP Ni-P (This work)	**52**	**96**	**32.9**	**4.1**
amorphous Ni-P [19]	115	170	57.0	-
amorphous Ni-P [20]	200	350	-	-
NiPx [21]	120 mV for obtaining 40mA/cm^2		-	-
Ni-P/Cu foam [22]	98	150	55.0	5.0
Ni-P/Ni foam [23]	80	140	50	3.2
PSD_Ni-10P [24]	105	230	44.7	0.55
CuO@Ni-P/CF [25]	73	160	72.0	2.9
Ni-Cu-P [26]	120	175	69	21

Double-layer capacitance measurement

Electrochemically active surface area was estimated by measuring a double-layer capacitance. To measure the electrochemical double-layer capacitance, the open circuit potential (OCP) was obtained in 1 M KOH. Then, the potential was swept between ±0.05 V vs OCP five times at each scan rates (10, 20, 40, 60, 80, 100, 200, 400 mV/s). The electrode was held at both potential vertexes for 10 seconds before conducting the next sweep to minimize the effect of the double-layer formed during the previous seep on the measured current. The measured capacitive currents were plotted as a function of scan rate and a slope showed the specific capacitance which can be converted to ECSA.

Calculation of electrochemically active surface area (ECSA)

We assumed 60 uF/cm^2 for the double-layer capacitance of theoretically flat Ni by previous reports.[3, 27]

Eq. S1:
$$A_{ECSA}^{Ni-P} = \frac{1.49 \times 10^3\ \mu F\ cm^{-2}}{60\ \mu F\ cm^{-2}} = 24.8\ cm_{ECSA}^2$$

Eq. S2:
$$A_{ECSA}^{Ni} = \frac{2.06 \times 10^3\ \mu F\ cm^{-2}}{60\ \mu F\ cm^{-2}} = 34.3\ cm_{ECSA}^2$$

Turnover frequency (TOF) calculation.

We used following formula;

Eq. S3:
$$TOF = \frac{Current\ at\ a\ given\ overpotential\ (150\ mV)}{Electron\ number \times Faraday\ constant \times Catalytic\ sites}\ (s^{-1})$$

We assumed the number of surface sites per surface area for Ni;

Eq. S4:
$$\#\ surface\ sites = \left(\frac{2\ atoms/unit\ cell\ surface}{3.52\ \text{Å}^2/unit\ cell\ surface}\right) = 1.614 \times 10^{15}/cm^2$$

(a) Electron number: 2 (For HER)

(b) Faraday constant: 96485 C mol^{-1}

(c) The number of Ni atoms on the surface of the electrode (n)

$= \left(1.614 \times 10^{15}\right) \times A_{ECSA}$

The calculated values are in manuscript.

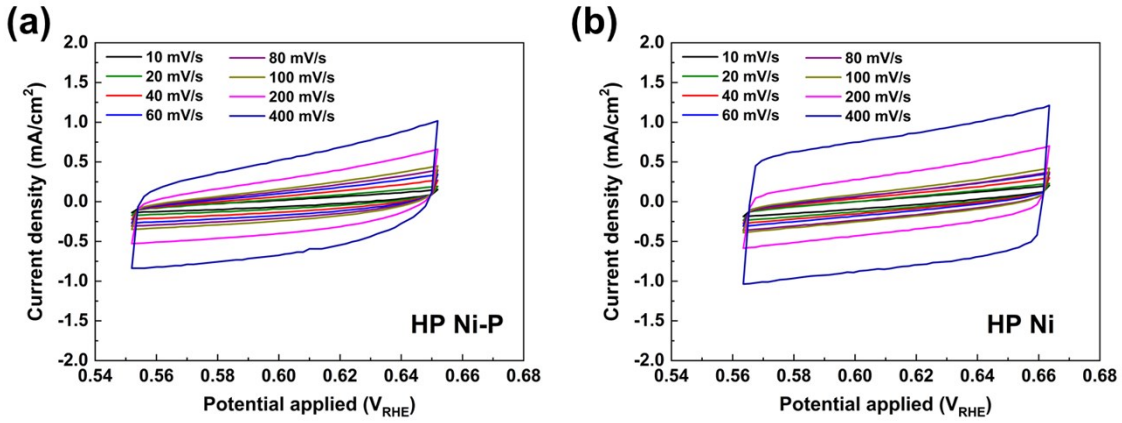

Figure S14. Cyclic voltammograms measured at scan rate from 10 to 400 mV/s for (a) the HP Ni-P and (b) the HP Ni.

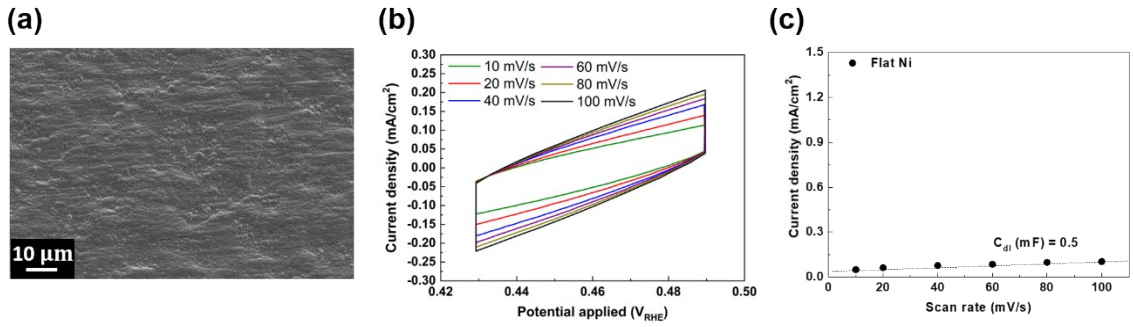

Figure S15. (a) SEM image of flat Ni surface, (b) Cyclic voltammograms for flat Ni measured at scan rate from 10 to 100 mV/s, and (c) corresponding capacitive current vs. scan rates plot.

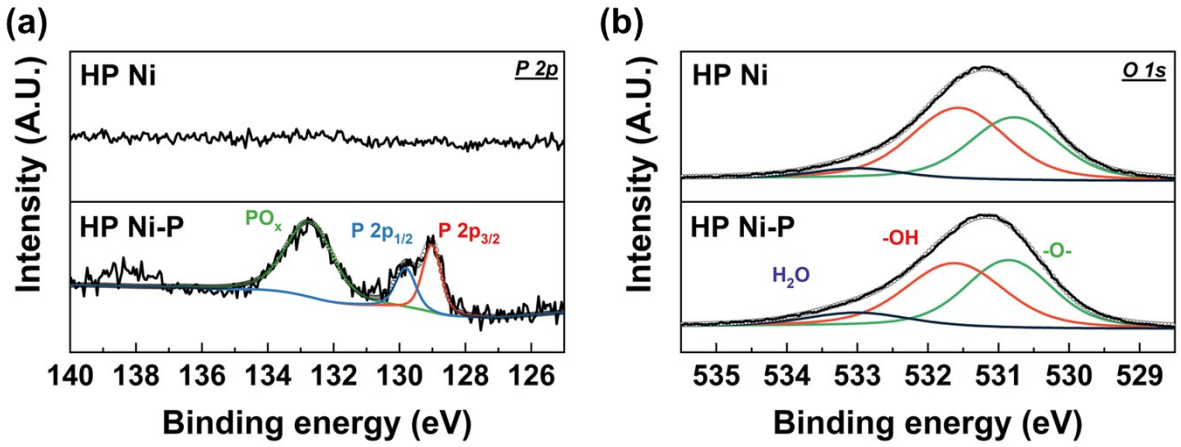

Figure S16. XPS results of (a) P 2p and (b) O 1s spectra of the HP Ni and HP Ni-P after HER.

Table S3. XPS peak area ratios of Ni^0, NiO and $Ni(OH)_2$/NiOOH to total Ni in HP Ni-P and HP Ni after 10 HER cycles.

	HP Ni-P	**HP Ni**
Ni^0	0.4208	0.2142
NiO	0.1150	0.1334
$Ni(OH)_2$/NiOOH	0.4642	0.6524

Evaluation of the amount of Ni^0 on the surface of the catalysts.

In order to obtain an oxidative charge of an initial Ni^0, as-deposited HP Ni-P and HP Ni were transferred to 1 M KOH immediately with minimal air exposure and oxidized at $0.6V_{RHE}$ for 200s under Ar atmosphere. To measure an oxidative charge of Ni^0 after HER, the HP Ni-P and HP Ni after 10 HER cycles were kept in an open-circuit state for 60s to eliminate adsorbed hydrogen during HER and then oxidized at $0.6V_{RHE}$ in Ar-purged 1 M KOH.

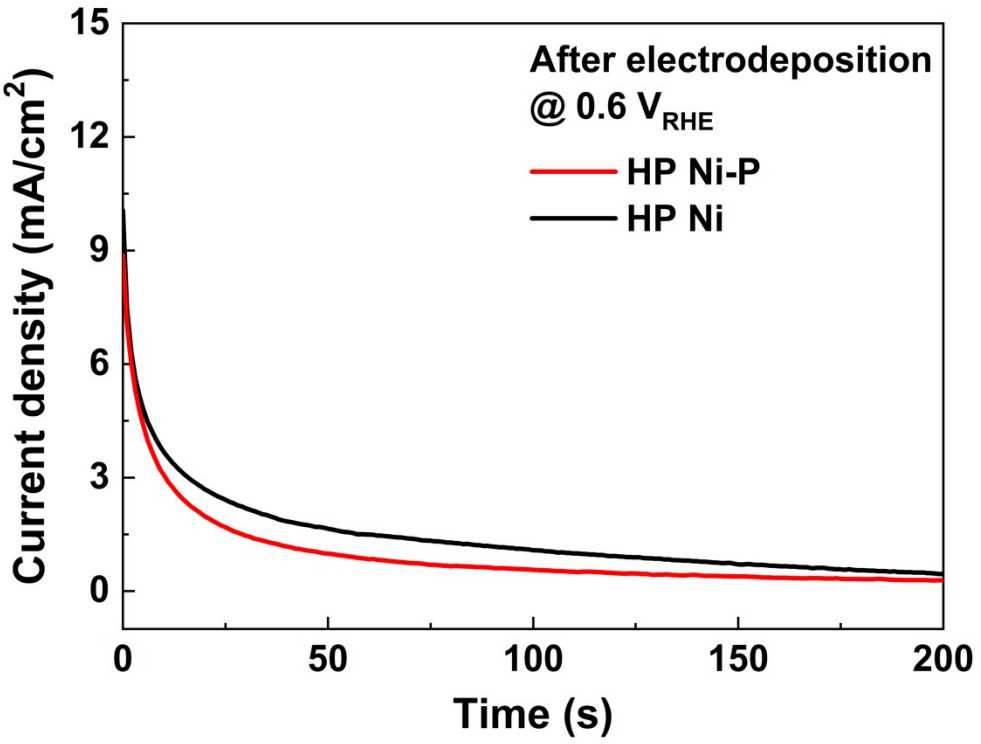

Figure S17. The i-t curves of as deposited HP Ni-P and HP Ni at $0.6V_{RHE}$.

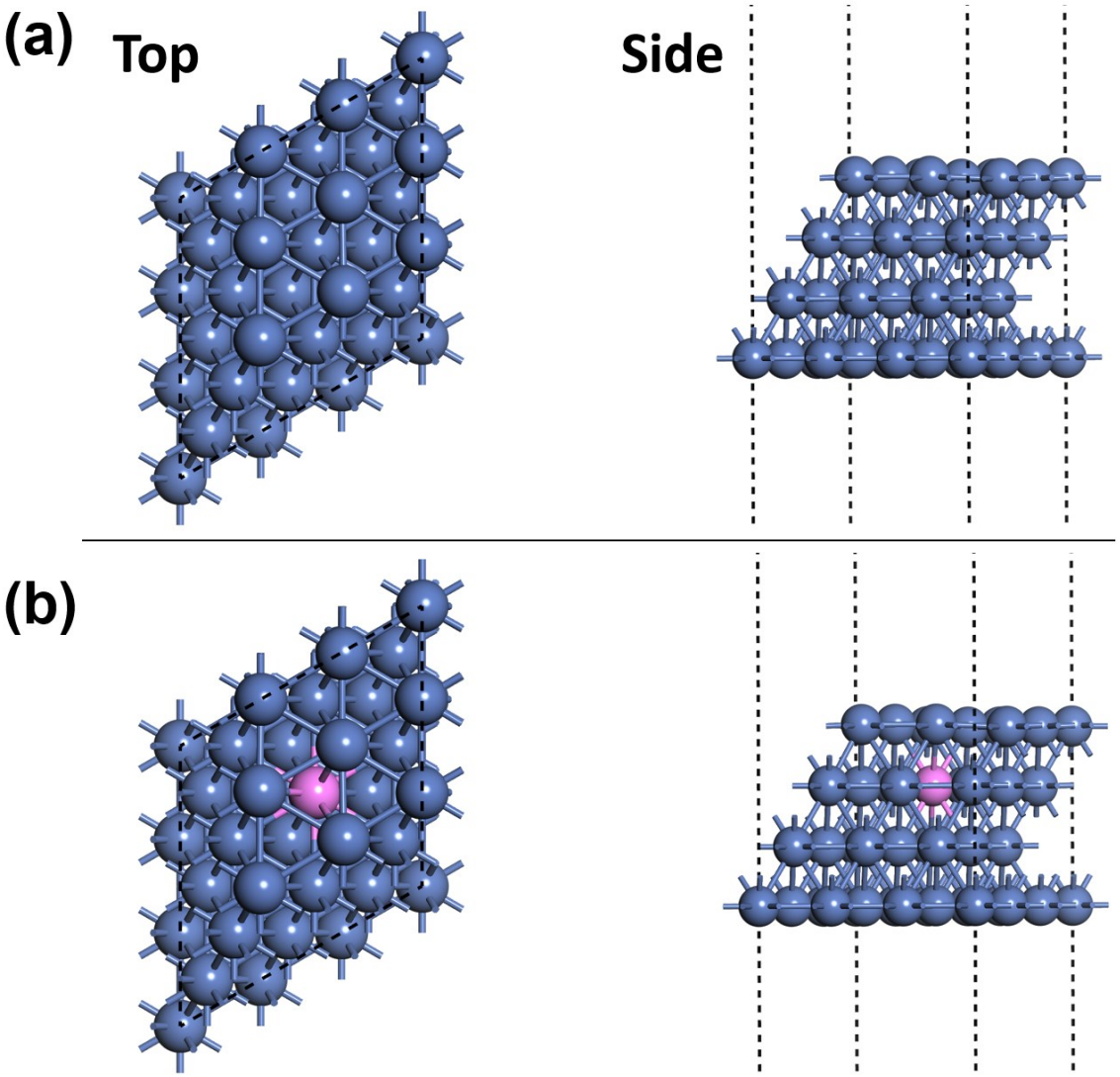

Figure S18. Top and side view of (a) Ni (111) and (b) Ni-P (111) models for the DFT calculation. Blue balls: Ni, Pink ball: P.

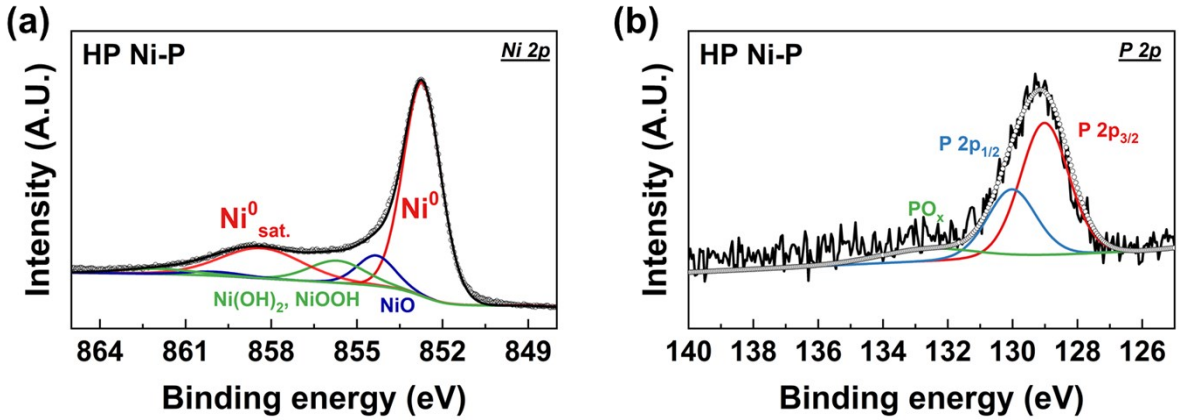

Figure S19. XPS spectra of the HP Ni-P after etching the surface layer: (a) Ni 2p and (b) P 2p (Ar sputter condition: 2keV, 1μA, 30sec, etching depth: about 2 nm)

Table S4. Calculated free energies of OH and H adsorption.

OH adsorption energy		
site	**Ni (111)**	**Ni-P (111)**
TOP	1.853	1.545 (T1)
		1.106 (T2)
		0.631 (T3)
		0.654 (T4)
		1.057 (T5)
HCP	0.071	0.100 (H1)
		0.152 (H2)
		0.021 (H3)
		0.054 (H4)
FCC	-0.028	-0.020 (F1)
		0.045 (F2)
		-0.008 (F3)
		-0.010 (F4)
H adsorption energy		
TOP	0.030	2.370
		0.160
		0.137
		0.160
		0.137
HCP	-0.539	-0.433
		-0.416
		-0.497
		-0.475
FCC	-0.555	-0.459
		-0.448
		-0.441
		-0.441

*Figure S15 shows the adsorption sites for Ni (111) and Ni-P (111)

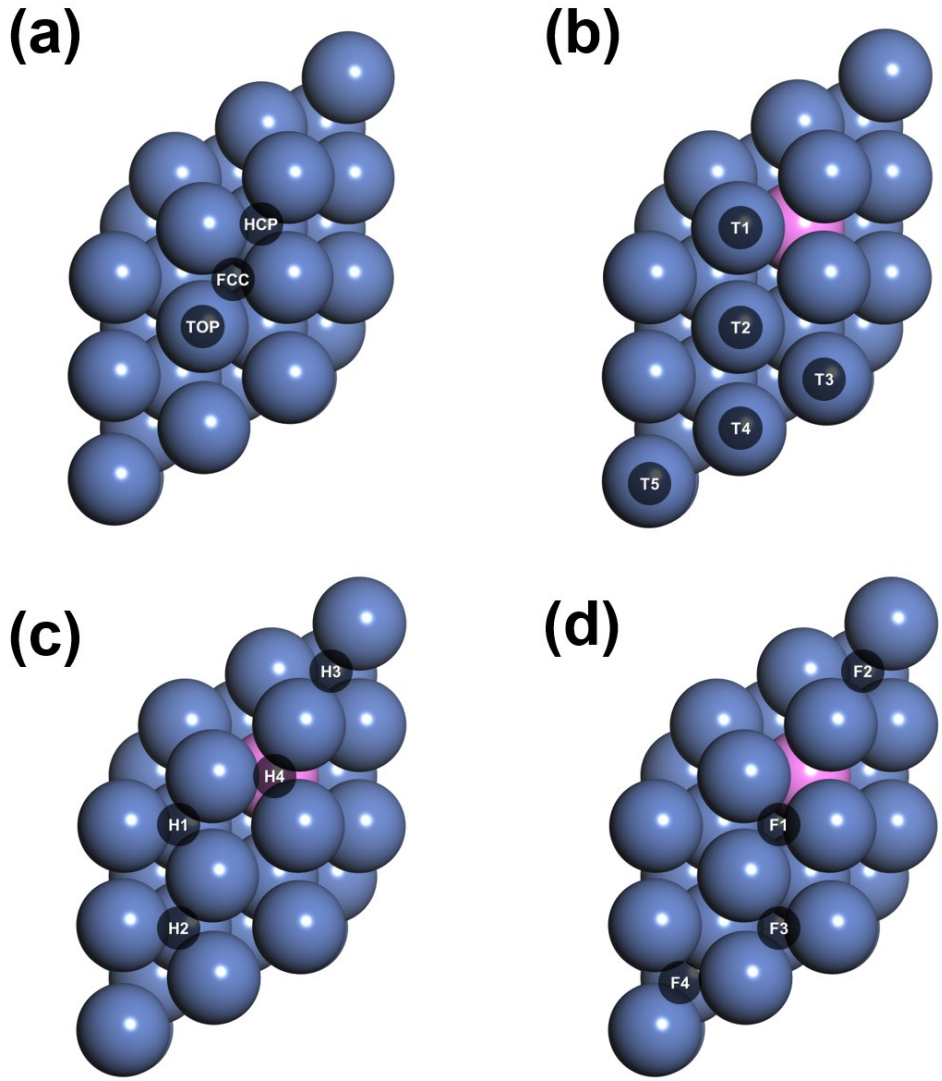

Figure S20. Possible adsorption sites for OH and H adsorption on the (a) Ni (111) and (b)-(d) Ni-P (111) surface. (top, hollow-hcp and hollow-fcc)

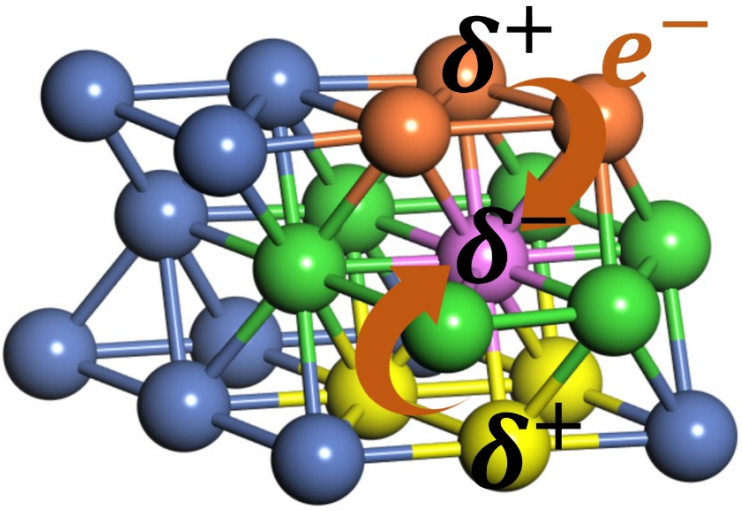

1st neighbor	Bader charge difference
1st layer	-0.01953 -0.03438 -0.01389
2nd layer	-0.01618 -0.03863 -0.03801 -0.01995 -0.03295 -0.01908
3rd layer	-0.03169 -0.01099 -0.01952
P atom	0.26128

Figure S21. Schematic charge transfer of the Ni-P (111) system calculated using Bader charge analysis. Orange, green, yellow-colored Ni atoms represent first-neighbor Ni atoms of the P atom on 1st layer, 2nd layer, and 3rd layer, respectively.

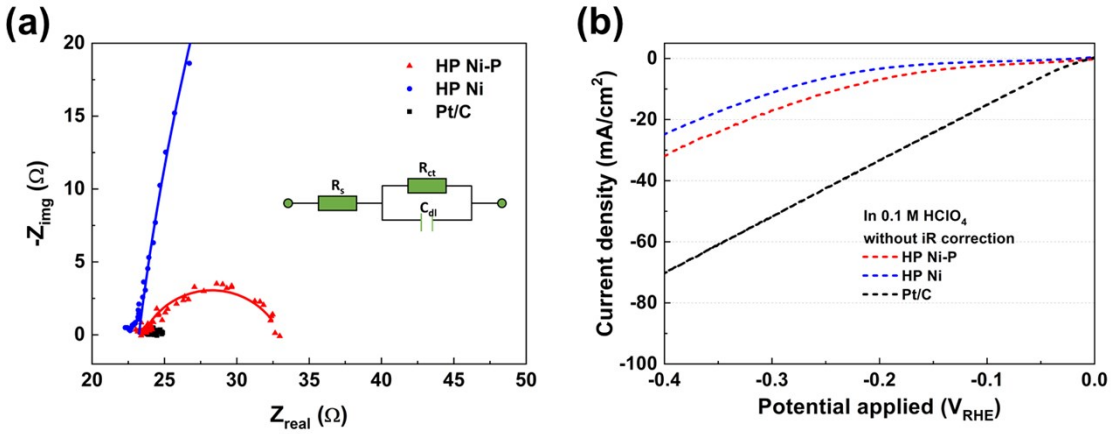

Figure S22. (a) Nyquist plots at -0.1 V_{RHE} and (b) HER polarization curves of the HP Ni-P, HP Ni, and commercial Pt/C in 0.1 M $HClO_4$ without iR correction.

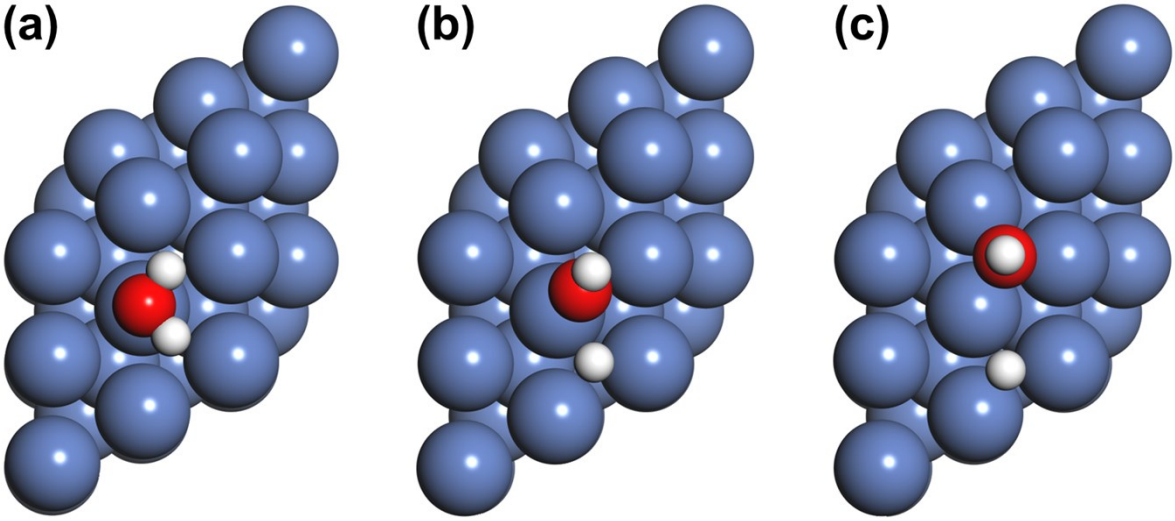

Figure S23. The detailed models of Ni (111) with (a) H_2O adsorption, (b) activated H_2O adsorption, and (c) OH and H adsorption.

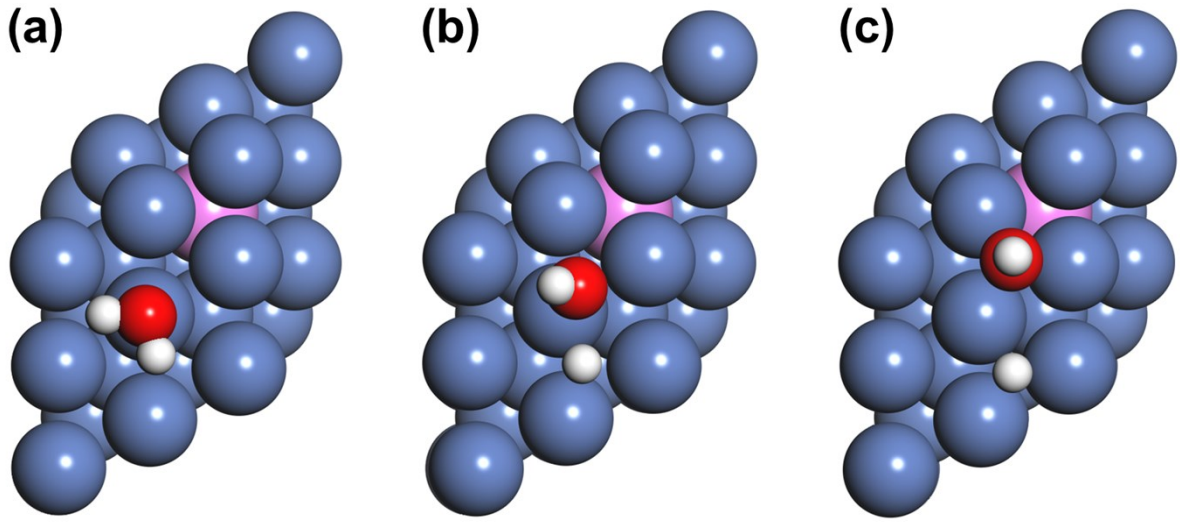

Figure S24. The detailed models of Ni-P (111) with (a) H_2O adsorption, (b) activated H_2O adsorption, and (c) OH and H adsorption.

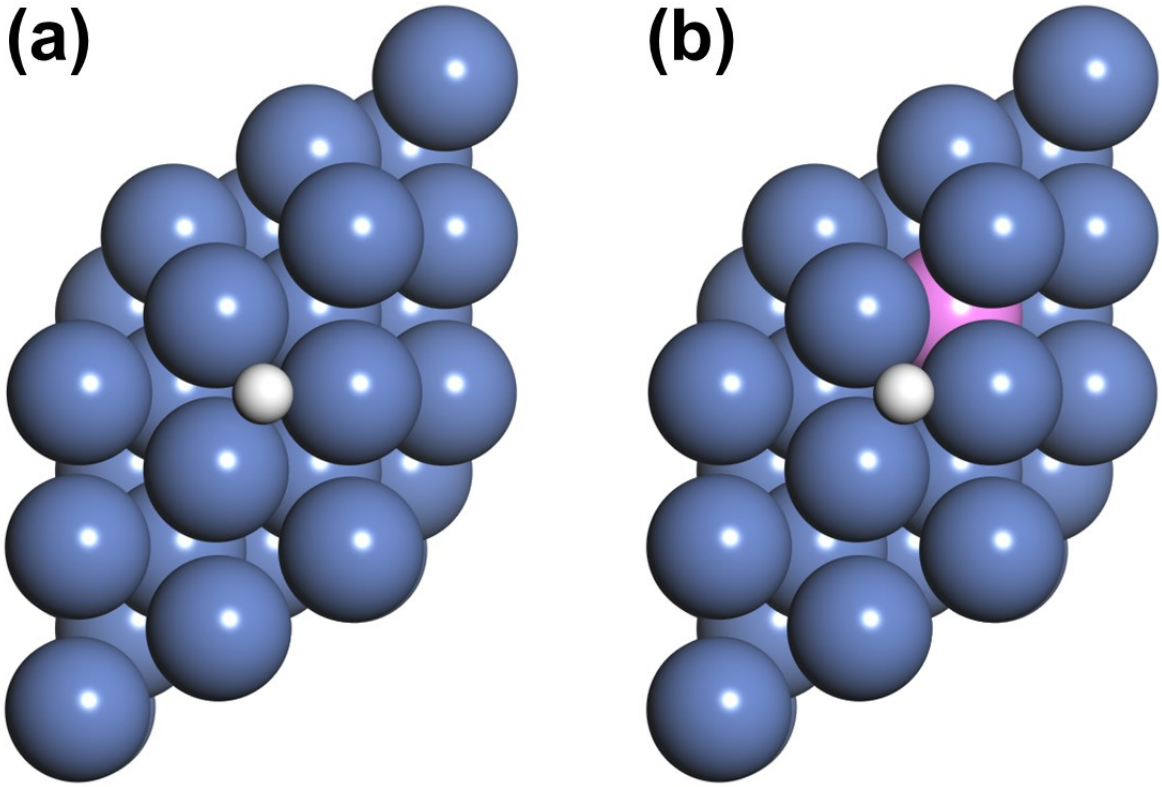

Figure S25. The detailed models of (a) Ni (111) with H adsorption, and (b) Ni-P (111) with H adsorption.

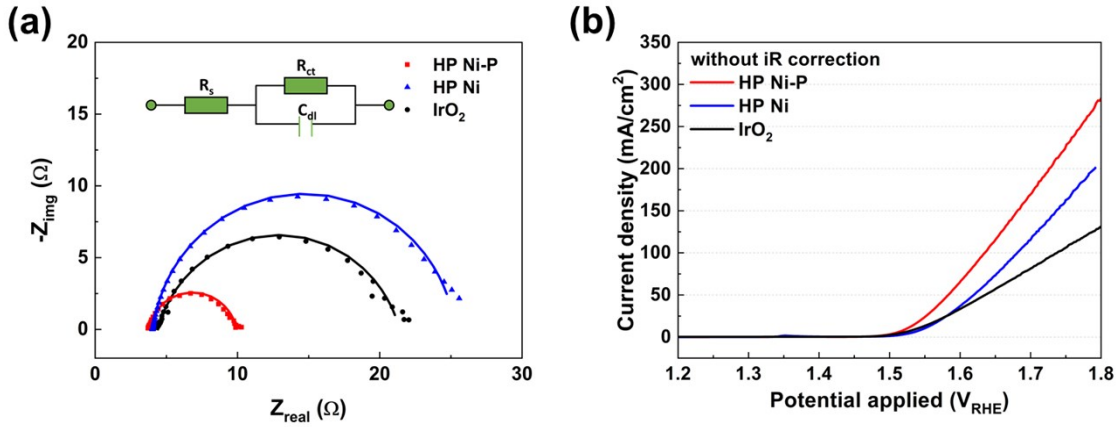

Figure S26. (a) Nyquist plots at 1.53 V_{RHE} and (b) OER polarization curves of the HP Ni-P, HP Ni, and commercial IrO_2 in 1 M KOH without iR correction.

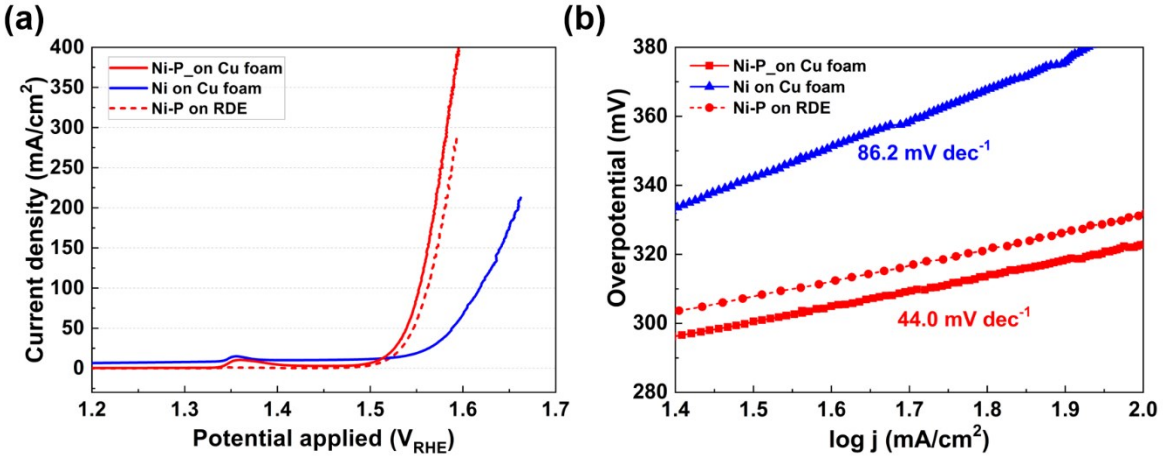

Figure S27. OER activities of the HP Ni-P deposited on Cu foam in 1 M KOH. (a) polarization curves, (b) corresponding Tafel plots.

Table S5. Comparison of OER catalytic activity and performance with the state-of-the-art bifunctional transition-metal phosphide or phosphorus catalysts.

Electrocatalyst	Overpotential (mV) at 10 mA/cm^2	Overpotential (mV) at 100 mA/cm^2	Tafel slope (mV/dec)	Electrolyte
HP Ni-P on foam (This work)	**279**	**323**	**44.0**	**1 M KOH**
HP Ni-P on RDE (This work)	286	331	39.5	1 M KOH
Ni_2P/rGO [5]	260	480	62	1 M KOH
np-$Ni_{0.67}Fe_{0.33}P_5$ [6]	245	580		1 M KOH
Porous Ni_2P [8]	320	-	106	1 M KOH
$Ni_{11}(HPO_3)_8(OH)_6$/NF [10]	245	280	102	1 M KOH
O_3-V_{10}-Ni_2P [11]	257	300	43.5	1 M KOH
$NiCo_2P_x$/CNT [12]	284	-	50.3	1 M KOH
Ni_2P/NF [13]	-	300	84.6	1 M KOH
$Ni_{1.85}Fe_{0.15}P$ NSAS/NF [14]	-	320	96	1 M KOH
Ni_2P/Ni/NF [15]	200	268	-	1 M KOH
Ni_2P/NF [16]	290	-	47	1 M KOH
Co-P foam [17]	300	-	74	1 M KOH
CoP/C [18]	360	-	66	0.1 M KOH

Table S6. OER activities of the electrodeposited Ni-P catalysts.

Electrocatalyst	Overpotential at 10 mA/cm^2 (mV)	Overpotential at 100 mA/cm^2 (mV)	Tafel slope (mV/dec)	Loading amount (mg/cm^2)
HP Ni-P (This work)	**279**	**323**	**44.0**	**4.1**
Ni-P/Cu foam [22]	325	430	120.0	5.0
Ni-P/Ni foam [23]	309	390	58.0	3.2
CuO@Ni-P/CF [25]	-	370	124.9	2.9

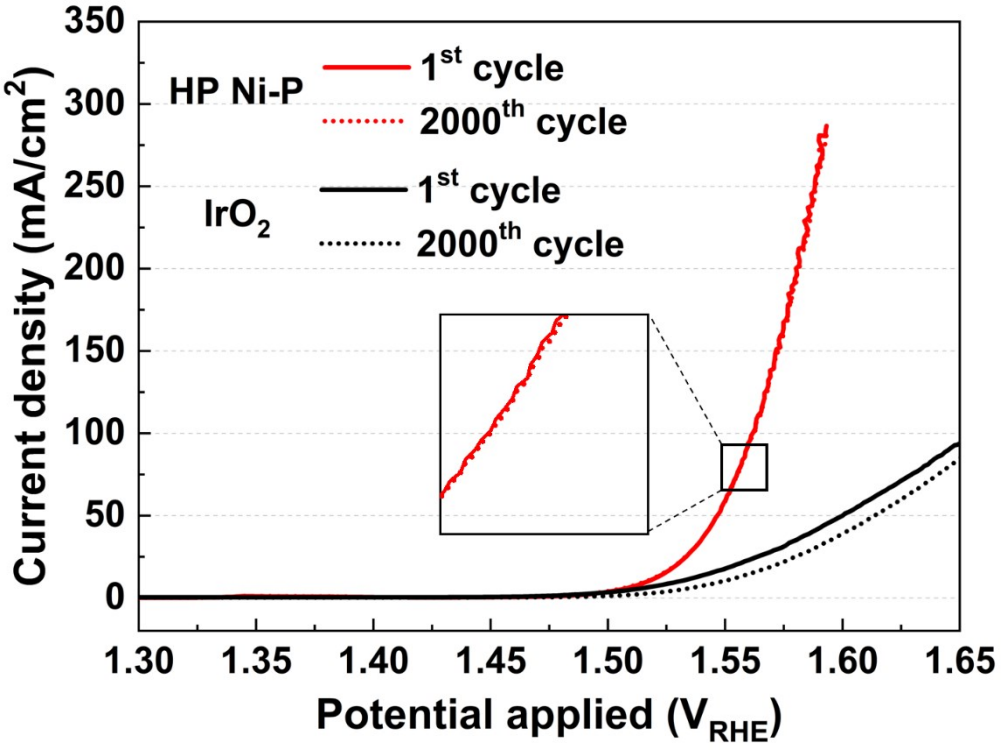

Figure S28. OER activities of the HP Ni-P and the IrO_2 before and after the potential cycling test from 1.3 to 1.7 V_{RHE} at a scan rate of 100 mV/s for 2000 cycles in 1 M KOH.

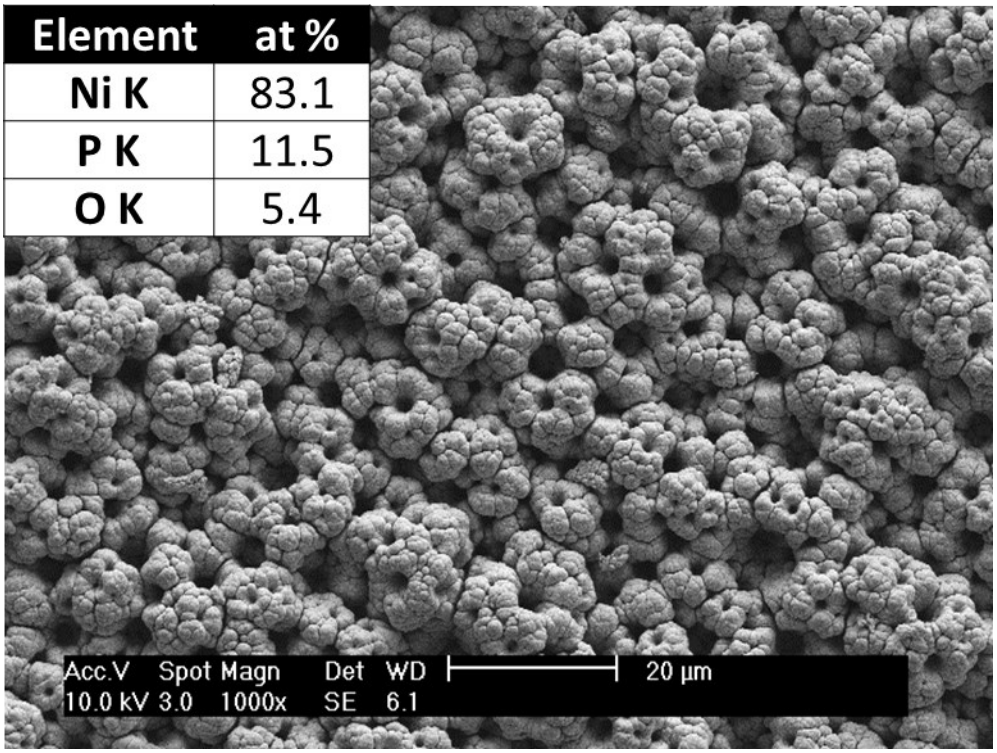

Figure S29. SEM image and elemental composition of the HP Ni-P after 10 h chronopotentiometry test at 100 mA/cm^2.

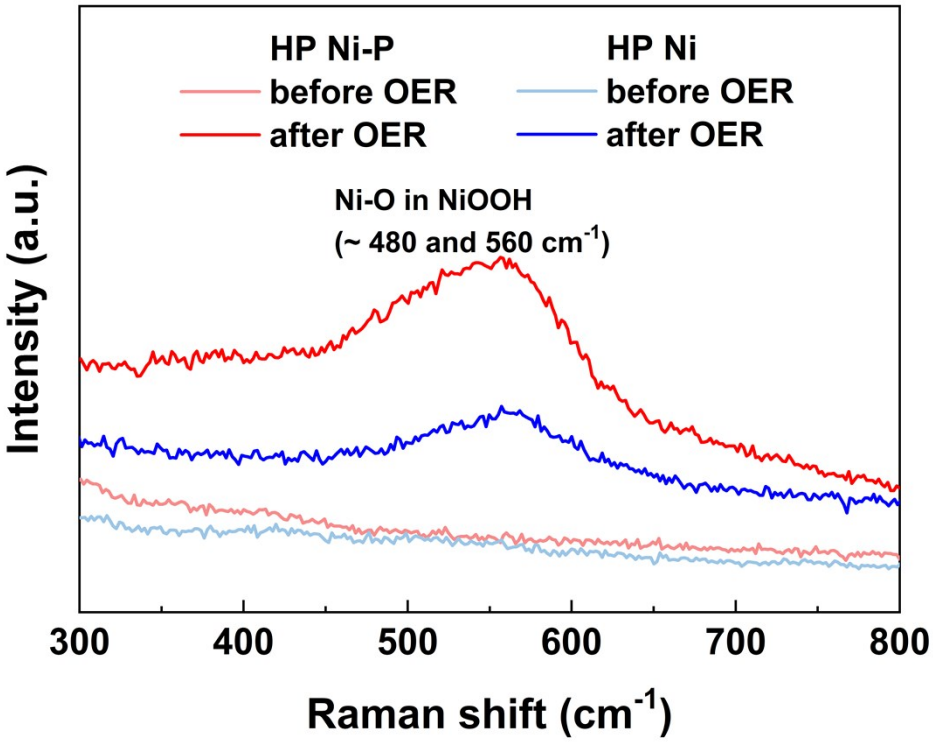

Figure S30. Raman spectra of the HP Ni-P and HP Ni before and after OER.

Table S7. Elemental composition of Ni, O, and P for HP Ni-P and HP Ni after 50 OER cycles obtained from XPS analysis.

	Ni %	**O %**	**P %**
Pristine	44.32	46.39	9.29
After HER	32.85	60.07	7.08
After OER	25.55	74.45	-

Determination of phosphate

To demonstrate the dissolution mechanism of phosphorus during OER, a simple qualitative method was adopted to determine the presence of phosphate ions in a 1 M KOH-after OER. The method involves the molybdenum blue formation reaction;

$PO_4^{3-} + 12(NH_4)2MoO_4 + 24H^+ \rightarrow (NH_4)_3PO_4 \cdot 12MoO_3 + 21NH_4^+ + 12H_2O$

$(NH_4)_3PO_4 \cdot 12MoO_3 + (N_2H_4 \cdot H_2O) \rightarrow$ molybdenum blue

The absorbance of formed molybdenum blue is measured from 800 to 900 nm. λ_{max}, presented between 800 to 900 nm, means the presence of phosphate in the solution.

The detection solution was prepared by modifying previous reports.[28, 29] To obtain 1 M KOH–after OER enriched with phosphate ion, twenty HP Ni-P electrodes were used for oxygen evolution reaction in 50 ml of 1 M KOH. The obtained 1 M KOH was acidified with 5 M H_2SO_4. Then, all solution was mixed and the absorbances of solution was measured by UV-Vis spectrophotometer. For comparison, the absorbance of as-prepared 1 M KOH was also measured.

In Fig. S19, λ_{max} was observed around 850-860 nm indicating the presence of phosphate ion in the 1 M KOH–after OER.

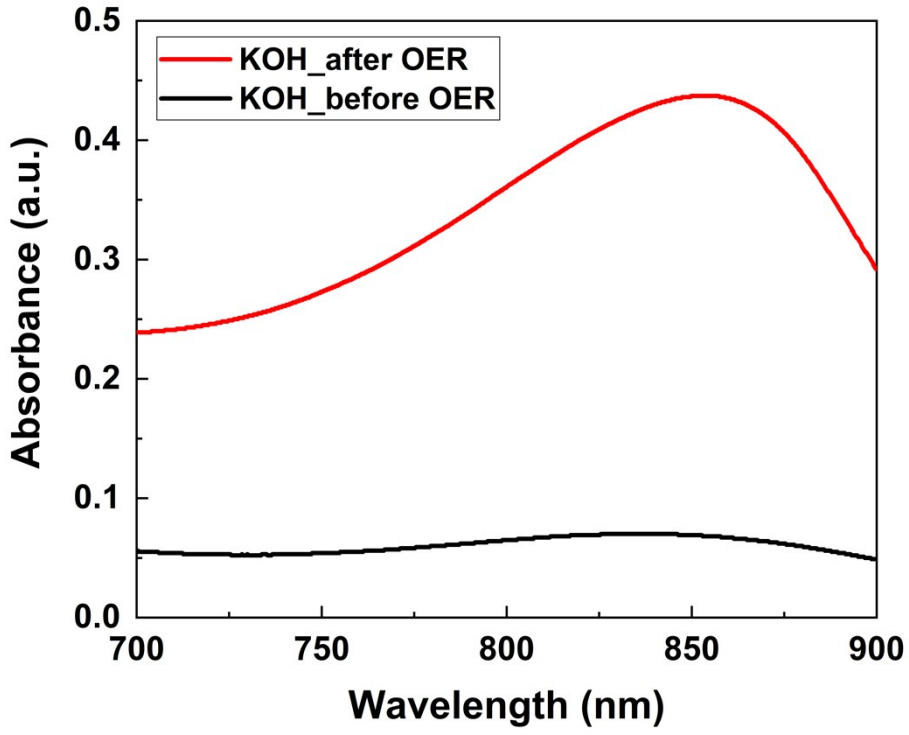

Figure S31. UV-Vis absorption spectra of (a) 1 M KOH used for OER of 20 HP Ni-P electrodes, (b) as prepared 1 M KOH.

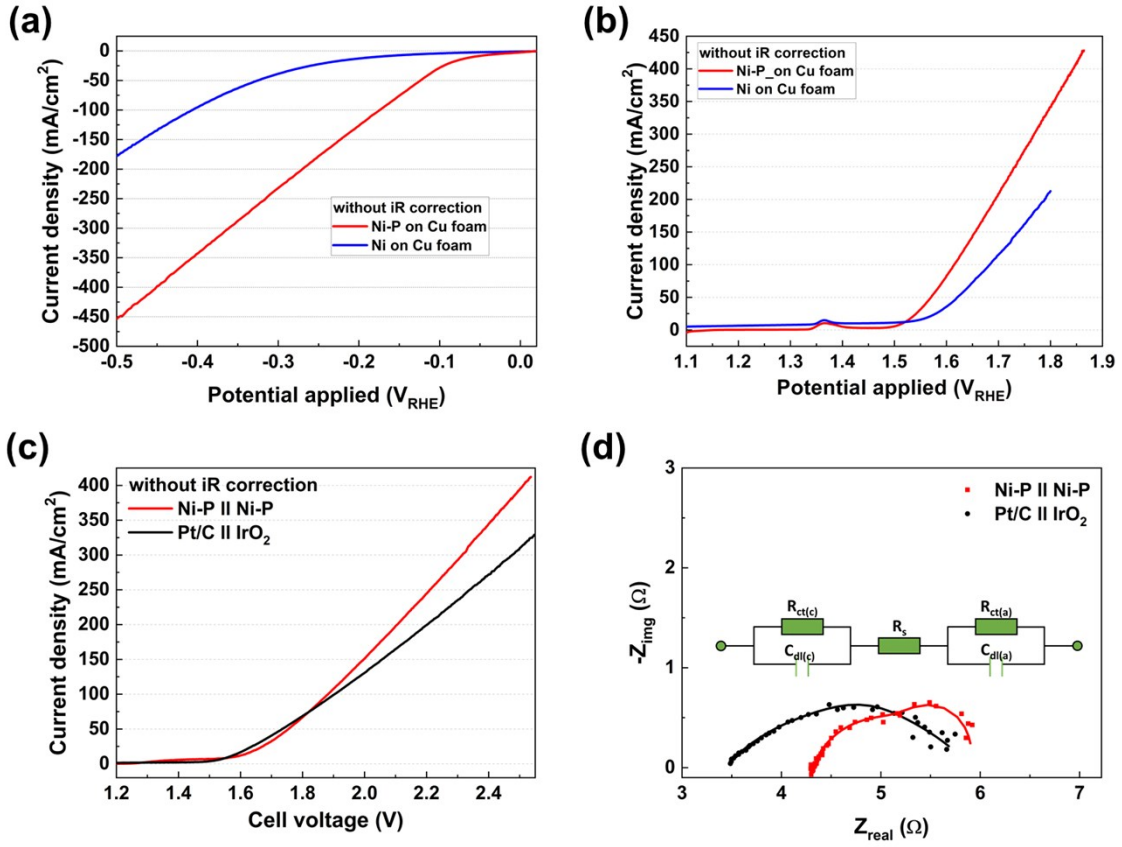

Figure S32. Polarization curves of the Ni-P and Ni on Cu foams without iR correction for (a) HER and (b) OER in 1 M KOH. (c) Water electrolysis performance without iR correction and (d) Nyquist plots at 1.8 V of the Ni-P || Ni-P and Pt/C || IrO_2 cells in 1 M KOH.

Table S8. Cell voltages of the Ni-P ‖ Ni-P and Pt/C ‖ IrO_2 electrolyzer at current densities of 20, 50, 100 and 200 mA/cm^2 measured from their polarization curves and chronopotentiometric curves in Fig. 5.

		Ni-P ‖ Ni-P			**Pt/C ‖ IrO_2**		
		Polarization curve	Chronopotentiometric curve		Polarization curve	Chronopotentiometric curve	
			Starting point*	Ending point*		Starting point*	Ending point*
Cell Voltage (V)	**20 mA/cm^2**	1.611	1.616	1.612	1.574	1.571	1.589
	50 mA/cm^2	1.657	1.653	1.653	1.630	1.681	1.697
	100 mA/cm^2	1.687	1.678	1.681	1.694	1.780	1.792
	200 mA/cm^2	1.715	1.707	1.707	1.780	1.903	2.109

*: The cell voltages were measured from the starting point and ending point of the chronopotentiometric curves at each current density section.

Reference

1. Y.-C. Chu, C.-J. Chang, Y. Zhu, S.-C. Lin, C.-W. Tung, T.-L. Chen and H. M. Chen, *ACS Sustainable Chemistry & Engineering*, 2019, **7**, 14247-14255.
2. L. Zhang, X. Wang, X. Zheng, L. Peng, J. Shen, R. Xiang, Z. Deng, L. Li, H. Chen and Z. Wei, *ACS Applied Energy Materials*, 2018, **1**, 5482-5489.
3. L. Yu, I. K. Mishra, Y. Xie, H. Zhou, J. Sun, J. Zhou, Y. Ni, D. Luo, F. Yu and Y. Yu, *Nano Energy*, 2018, **53**, 492-500.
4. F. Yu, H. Zhou, Y. Huang, J. Sun, F. Qin, J. Bao, W. A. Goddard III, S. Chen and Z. Ren, *Nature communications*, 2018, **9**, 2551.
5. L. Yan, H. Jiang, Y. Xing, Y. Wang, D. Liu, X. Gu, P. Dai, L. Li and X. Zhao, *Journal of Materials Chemistry A*, 2018, **6**, 1682-1691.
6. W. Xu, S. Zhu, Y. Liang, Z. Cui, X. Yang and A. Inoue, *Journal of Materials Chemistry A*, 2018, **6**, 5574-5579.
7. M. Wu, P. Da, T. Zhang, J. Mao, H. Liu and T. Ling, *ACS Appl. Mater. Interfaces*, 2018, **10**, 17896-17902.
8. Q. Wang, Z. Liu, H. Zhao, H. Huang, H. Jiao and Y. Du, *Journal of Materials Chemistry A*, 2018, **6**, 18720-18727.
9. J. Mu, J. Li, E.-C. Yang and X.-J. Zhao, *ACS Applied Energy Materials*, 2018, **1**, 3742-3751.
10. P. W. Menezes, C. Panda, S. Loos, F. Bunschei-Bruns, C. Walter, M. Schwarze, X. Deng, H. Dau and M. Driess, *Energy Environ. Sci.*, 2018, **11**, 1287-1298.
11. K. N. Dinh, X. Sun, Z. Dai, Y. Zheng, P. Zheng, J. Yang, J. Xu, Z. Wang and Q. Yan, *Nano Energy*, 2018, **54**, 82-90.
12. C. Huang, T. Ouyang, Y. Zou, N. Li and Z.-Q. Liu, *Journal of Materials Chemistry A*, 2018, **6**, 7420-7427.
13. X.-D. Wang, Y. Cao, Y. Teng, H.-Y. Chen, Y.-F. Xu and D.-B. Kuang, *ACS Appl. Mater. Interfaces*, 2017, **9**, 32812-32819.
14. P. Wang, Z. Pu, Y. Li, L. Wu, Z. Tu, M. Jiang, Z. Kou, I. S. Amiinu and S. Mu, *ACS Appl. Mater. Interfaces*, 2017, **9**, 26001-26007.
15. B. You, N. Jiang, M. Sheng, M. W. Bhushan and Y. Sun, *ACS Catalysis*, 2016, **6**, 714-721.
16. L.-A. Stern, L. Feng, F. Song and X. Hu, *Energy Environ. Sci.*, 2015, **8**, 2347-2351.
17. S. Oh, H. Kim, Y. Kwon, M. Kim, E. Cho and H. Kwon, *Journal of Materials Chemistry A*, 2016, **4**, 18272-18277.
18. J. Ryu, N. Jung, J. H. Jang, H.-J. Kim and S. J. Yoo, *Acs Catalysis*, 2015, **5**, 4066-4074.
19. I. Paseka, *Electrochimica Acta*, 1995, **40**, 1633-1640.
20. I. Paseka, *Electrochimica acta*, 1999, **44**, 4551-4558.
21. T. Burchardt, *Int. J. Hydrog. Energy*, 2001, **26**, 1193-1198.
22. Q. Liu, S. Gu and C. M. Li, *Journal of Power Sources*, 2015, **299**, 342-346.
23. C. Tang, A. M. Asiri, Y. Luo and X. Sun, *ChemNanoMat*, 2015, **1**, 558-561.
24. C. Sun, J. Zeng, H. Lei, W. Yang and Q. Zhang, *ACS Sustainable Chemistry & Engineering*, 2018, **7**, 1529-1537.
25. B. Chang, S. Hao, Z. Ye and Y. Yang, *Chemical Communications*, 2018, **54**, 2393-2396.
26. M. Cao, Z. Xue, J. Niu, J. Qin, M. Sawangphruk, X. Zhang and R. Liu, *ACS Appl. Mater. Interfaces*, 2018, **10**, 35224-35233.

27. J. Kibsgaard, C. Tsai, K. Chan, J. D. Benck, J. K. Nørskov, F. Abild-Pedersen and T. F. Jaramillo, *Energy Environmental Science*, 2015, **8**, 3022-3029.
28. M. Kumar, M. S. A. Galil, M. Suresha, M. Sathish and G. Nagendrappa, *Journal of Chemistry*, 2007, **4**, 467-473.
29. S. Pradhan and M. R. Pokhrel, *Scientific world*, 2013, **11**, 58-62.